A Free-Standing and Ultralong-Life Lithium-Selenium Battery Cathode Enabled by 3D Mesoporous Carbon/Graphene Hierarchical Architecture

Kai Han, Zhao Liu, Jingmei Shen, Yuyuan Lin, Fang Dai,* and Hongqi Ye*

High capacity cathode materials for long-life rechargeable lithium batteries are urgently needed. Selenium cathode has recently attracted great research attention due to its comparable volumetric capacity to but much better electrical conductivity than widely studied sulfur cathode. However, selenium cathode faces similar issues as sulfur (i.e., shuttling of polyselenides, volumetric expansion) and high performance lithium-selenium batteries (Li–Se) have not yet been demonstrated at selenium loading >60% in the electrode. In this work, a 3D mesoporous carbon nanoparticles and graphene hierarchical architecture to storage selenium as binder-free cathode material (Se/MCN-RGO) for high energy and long life Li–Se batteries is presented. Such architecture not only provides the electrode with excellent electrical and ionic conductivity, but also efficiently suppresses polyselenides shuttling and accommodates volume change during charge/discharge. At selenium content of 62% in the entire cathode, the free-standing Se/MCN-RGO exhibits high discharge capacity of 655 mAh g^{-1} at 0.1 C (97% of theoretical capacity) and long cycling stability with a very small capacity decay of 0.008% per cycle over 1300 cycles at 1 C. The present report demonstrates significant progress in the development of high capacity cathode materials for long-life Li batteries and flexible energy storage device.

1. Introduction

In recent years, developing novel high capacity cathode materials for lithium (Li) batteries have attracted increasing attention due to the tremendous demands of high-energy battery systems for electric vehicles (EV).[1,2] Oxygen and sulfur have gained enormous attention to be alternative cathode materials for rechargeable Li–air and Li–S batteries due to their higher theoretical capacities in contrast to conventional metal oxides and phosphates cathode materials.[3–9] However, both oxygen and sulfur severely suffer from low electrical conductivity and poor cycling stability, which significantly hinder their practical applications.[10–13]

Selenium (Se), a d-electron containing element from same group as oxygen and sulfur in the periodic table, has been widely studied as electrode materials for solar cells.[14,15] However, the exploration of selenium as cathode material for rechargeable lithium batteries is still in a very preliminary stage. When used as the cathode material for Li batteries, selenium can provide high theoretical gravimetric capacity (678 mAh g^{-1}) and volumetric capacity (3268 mAh cm^{-3}).[16] Moreover, selenium possesses much higher electrical conductivity (1×10^{-3} S m^{-1}, approximately 20 orders of magnitude) than that of sulfur, potentially giving it the promise of higher capacity utilization and rate capability.[17] Most recently, Abouimrane et al. have successfully applied selenium as cathode material for both Li-ion and Na-ion batteries.[18,19] The results indicate that even the bulk selenium showed higher electrochemical activity, especially in the cycling stability, than sulfur.[18,19] However, similar to sulfur, the dissolution and shuttling of lithium polyselenides, together with significant volume change, are still present in ether-based electrolyte during electrochemical cycling.[18,20] To overcome these issues, several strategies have been reported, such as confinement of selenium in porous carbon,[16,21,22] adsorption of polyselenides by metal oxide,[23] insertion of carbon interlayer to adsorb soluble polyselenides,[24] and design of nanoporous or nanofibrous selenium structure.[25,26] Some other work has focused on the lithium metal anode to potentially improve the safety issue for Li–Se batteries.[27,28] Despite these efforts, improved electrochemical performance could only be achieved at relatively low selenium content.[21] While very low discharge capacity and poor cycling stability are observed for higher selenium content (Table S1, i.e., 200 mAh g^{-1} for 20 cycles at 0.15 C with 70% Se content).[25] To solve this challenging issue, inspired by the reported successful strategies for sulfur and silicon materials,[29–34] it is believed that the elaborate design of electrode architecture would be critical to

K. Han, Prof. H. Ye
College of Chemistry and Chemical Engineering
Central South University
Changsha, Hunan 410083, P. R. China
E-mail: hankai@csu.edu.cn
Z. Liu, Dr. Y. Lin
Department of Material Science and Engineering
Northwestern University
Evanston, IL 60208, USA
Dr. J. Shen, Dr. F. Dai
Optimal CAE Inc.
Plymouth, MI 48170, USA
E-mail: daifang621@gmail.com

DOI: 10.1002/adfm.201402815

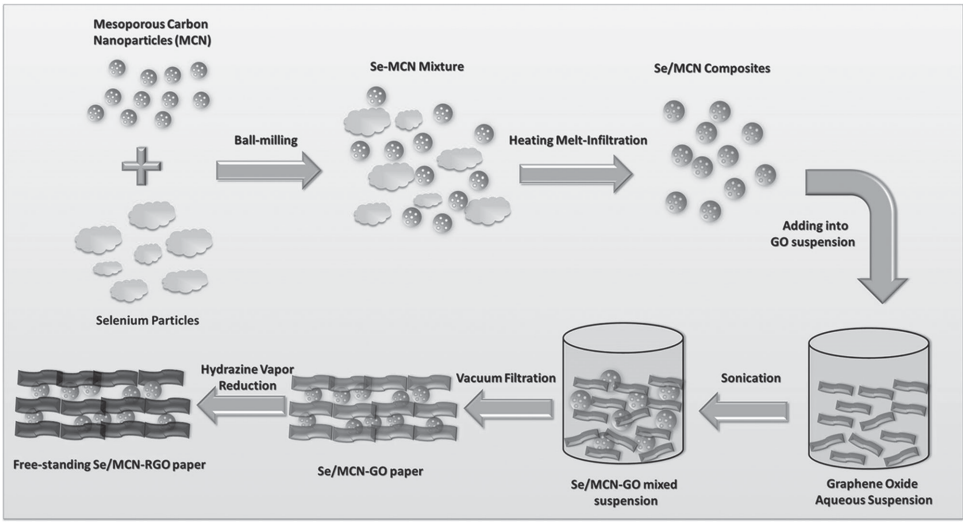

Figure 1. Scheme of the synthesis route of Se/MCN-RGO paper.

achieve the high capacity and long cycle life with high selenium loading for Li–Se batteries.

Herein, we strategically design and fabricate a free-standing selenium composite cathode material with a 3D hierarchical architecture, in which selenium is impregnated into the mesoporous carbon nanoparticles (Se/MCN), followed by further embedding in graphene sheets (Se/MCN-RGO). Our design of such 3D hierarchical carbon architecture was mainly based on the following assumptions: 1) confinement of polyselenides by MCN and further adsorption/reuse of escaped polyselenides by graphene sheets promising high capacity utilization and high efficiency; 2) 3D interconnected open channels constructed by MCN and graphene sheets as well as mesopores from MCN providing excellent electrical and ionic conductivity to ensure the high rate performance; 3) flexibility properties of 2D graphene sheets benefiting accommodation of the volume change and inhibition of the cathode structure fragmentation during long-term cycling; and 4) elimination of polymer binder and organic solvent during electrode preparation considerably minimizing the cost, and significantly increasing selenium overall content in the electrode. The experimental results from both materials characterization and electrochemical measurements validated all hypotheses above. The free-standing Se/MCN-RGO paper with 62% selenium delivered a high discharge capacity of 655 mAh g^{-1} at 0.1 C (1 C = 678 mA g^{-1} of Se), corresponding to 97% utilization of active material and the capacity retained 568 mAh g^{-1} after 100 cycles. Moreover, at a high current rate of 1 C, the Se/MCN-RGO electrode also demonstrated an ultra-long cycle life with 89% capacity retention after 1300 cycles, only 0.008% capacity decay for each cycle. To best of our knowledge, selenium-based cathode material with such high capacity and ultra-long cycle life at selenium content above 60% has not been reported yet (Table S1, Supporting Information). This excellent performance makes the free-standing Se/MCN-RGO composite a competitive cathode material for practical application in rechargeable long-life lithium batteries.

2. Results and Discussion

2.1. Synthesis and Structural Characterization

The free-standing Se/MCN-RGO composite was fabricated via a facile two-step process: heating melt-infiltration of selenium into MCN together with assembly and reduction of Se/MCN-GO paper by hydrazine monohydrate vapor (**Figure 1**). The field-emission scanning electron microscope (FESEM) images of the products obtained at different preparation stages are shown in Figure S1 (Supporting Information). The particle size of pristine MCN is about 50 nm and selenium exists as agglomeration of ≈1–2 µm. It is expected that the nano-sized mesoposrous carbon particles could be effectively embedded in graphene sheets rather than micrometer-sized mesoporous carbon particles.[21,35,36] In addition, the nano-sized particles could further shorten the lithium ion pathway and consequently enhance the rate performance. After heating melt-infiltration at 260 °C, the bulk selenium agglomeration disappears (Figure S1g). Instead, selenium is uniformly distributed (Figure S1h) and confined in the mesopores (Figure S2) of MCN matrix. The Se/MCN nanoparticles were then homogeneously mixed with GO aqueous suspension and assembled by vacuum filtration to produce Se/MCN-GO paper (Figure S1i). Finally, the free-standing Se/MCN-RGO composite paper was obtained by hydrazine monohydrate vapor reduction at 130 °C. The final content of selenium active material in as-prepared Se/MCN-RGO paper is 62% determined by TGA (Figure S3). The morphologies of Se/MCN-RGO are shown in **Figure 2**. It is a free-standing paper with average thickness of ~ 50 µm and could be readily bend back and forth several times without breaking. Figure 2b,c shows the layered structure of Se/MCN-RGO. The Se/MCN is well embedded in graphene layers and only a few particles exposed on the outer surface. Transmission electron microscopy (TEM) images (Figure 2d,e and Figure S2c,d) reveal the confinement of selenium within the MCN and distribution of Se/MCN particle clusters in graphene sheets. The presence of Se/MCN successfully prevents graphene sheets

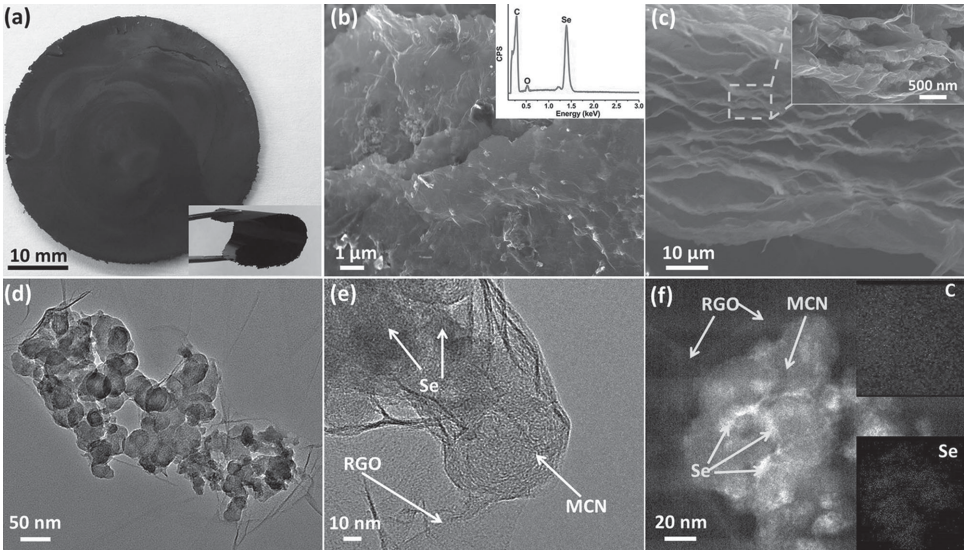

Figure 2. a) Digital photo of the free-standing Se/MCN-RGO paper electrode and bended with tweezer (inset). b) FESEM image of Se/MCN-RGO paper surface. Inset: the corresponding EDS spectrum. c) Cross-sectional FESEM and high-magnification FESEM (inset) images of Se/MCN-RGO paper. d,e) TEM images of Se/MCN-RGO at different magnifications. f) HAADF-STEM Z contrast image of Se/MCN-RGO and corresponding EDS mapping of Se and carbon.

from re-stacking during reduction process, resulting in the 3D interconnected open channels to enhance lithium ion transportation during cycling. Z contrast image by high-angle annular dark-field in scanning transmission electron microscopy (HAADF-STEM) and corresponding energy dispersive spectroscopy (EDS) selenium elemental mapping in Figure 2f further confirm the presence and uniform distribution of selenium in the hierarchical carbon matrix.

X-ray diffraction (XRD) analysis was conducted to understand the crystalline structure and composition change of products during Se/MCN-RGO preparation, as shown in **Figure 3**a. The crystalline structure of selenium is maintained after ball-milling mixed with MCN. However, the characteristic diffraction peaks of the selenium disappear after heating melt-infiltration, which partially indicates confinement of amorphous selenium in the mesopores of MCN.[16] The broadening of characteristic (002) diffraction peak for MCN at 26° is observed, probably due to the filling of amorphous selenium. It is noted that when incorporating Se/MCN with GO, the characteristic diffraction peak of GO slightly shifts from 11.4° to 10.4°, corresponding to an increase of interlayer spacing from 0.75 to 0.85 nm, confirming the insertion of Se/MCN into GO sheets. Disappearance of such GO peak in Se/MCN-RGO reveals complete reduction of GO to reduced graphene oxide (RGO) by hydrazine monohydrate vapor. The Se/MCN and Se/MCN-RGO were also characterized by Raman spectroscopy (Figure 3b) to further determine the structure of selenium and carbon in the composite materials. The pristine selenium only displays a sharp characteristic peak at 237 cm^{-1}, which is attributed to chain-structured selenium.[16,21] The absence of this peak in Se/MCN and Se/MCN-RGO indicates the crystalline to amorphous selenium transformation after the impregnation process into mesopores of MCN, which is consistent with the XRD results. Carbon could be characterized by the D band at ≈1350 cm^{-1} and G band at ≈1570 cm^{-1} corresponding to disorders/defects and graphitic degree, respectively.[29] The MCN is partially graphitized because of the presence of both D and G band and the intensity of D band is lower than G band. While the intensity ratio of D and G band increased in Se/MCN-RGO, suggesting the increase of disorders and defects, or reduction of sp^2 domains in the carbon matrix, which probably generated during the GO reduction process.[37]

Figure 3c presents the nitrogen sorption isotherms of the pristine MCN as well as that of the Se/MCN composite and the corresponding pore size distributions obtained by the Barrett-Joyner-Halenda (BJH) model (inset in Figure 3c) to investigate the surface area and porosity of the samples. A hysteresis loop is observed in the N_2 adsorption for pristine MCN, indicating the presence of mesopores in MCN. The Brunauer-Emmett-Teller (BET) specific surface area of the MCN is 241.4 $m^2\ g^{-1}$ and the total pore volume is 0.39 $cm^3\ g^{-1}$. The average pore diameter calculated by BJH is around 4 nm. After selenium infiltration, the hysteresis loop almost disappeared. The BET surface area and the total pore volume decrease to 11.3 $m^2\ g^{-1}$ and 0.09 $cm^3\ g^{-1}$, respectively. These results imply that selenium is impregnated into the MCN and mainly occupy the mesopores after the heating melt-infiltration process. (Figure 3c inset).

X-ray photoelectron spectroscopy (XPS) analysis was carried out to elucidate the chemical state of carbon and selenium in the composite and reduction degree of GO. Figure 3d,e shows the presence of elemental selenium in the Se/MCN-RGO paper. Evolution of C 1s peak (Figure S4b,d, Supporting Information) illustrates effective remove of oxygen-containing group during hydrazine monohydrate vapor reduction of GO. It is worth mentioning here that the nitrogen signal was detected in Se/MCN-RGO paper during XPS survey scan but not in Se/MCN-GO (Figure S4a). We attribute this to the reduction process by hydrazine monohydrate vapor, which has been demonstrated to leave nitrogen doping in the carbon matrix.[38] The XPS survey scan (Figure S4a) reveals about 5 at% nitrogen in the Se/MCN-RGO

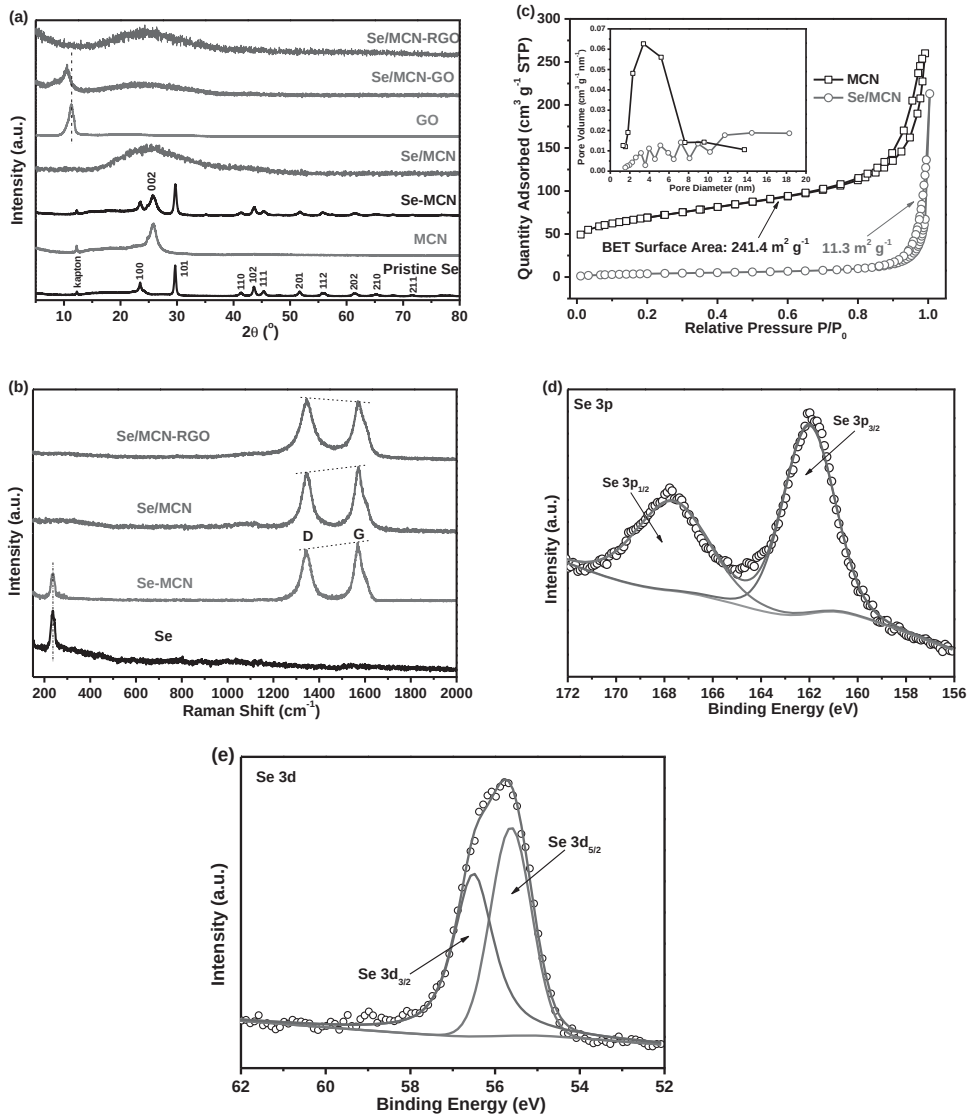

Figure 3. a) XRD patterns of pristine Se, Se/MCN-RGO and other products obtained at different steps during preparation. b) Raman spectra of Se, Se-MCN, Se/MCN, and Se/MCN-RGO. c) Nitrogen adsorption/desorption isotherms of MCN and Se/MCN. Inset: BJH pore size distribution plots. d) High-resolution XPS Se 3p and e) Se 3d spectra of Se/MCN-RGO.

paper and the high resolution N 1s spectrum (Figure S4d) could be fitted into three peaks corresponding to pyridinic N, pyrrolic N and quaternary N, respectively. The presence of nitrogen heteroatoms within the carbon matrix could further increase the electrical conductivity of the composite materials, which is benefiting the electrochemical performance.[39–42]

2.2. Electrochemical Evaluation

To evaluate the electrochemical performance of the Se/MCN-RGO composite material, Se/MCN-RGO paper was directly used as electrode and paired with lithium metal in a 2032-type coin cell without adding any inactive materials, such as polymer binder. We also prepared the Se/MCN and MCN-RGO electrodes to compare with as-obtained Se/MCN-RGO electrode and identify the capacity contribution from carbon matrix in the composite. **Figure 4**a shows a typical cyclic voltammetry (CV) of the Se/MCN-RGO cathode in the voltage range of 0.8–3.0 V at a scan rate of 0.1 mV s^{-1} for the first twenty cycles. In the first cathodic scan, three reduction peaks are observed, including a very small peak at 2.25 V, a peak at 2.15 V and a broader peak at 1.9 V, which correspond to the stepwise electrochemical reduction of selenium to polyselenides and finally to Li_2Se.[18] This is similar to the electrochemical process of its sulfur analogues.[43,44] The subsequent anodic scan shows a strong oxidation peak at 2.25 V with a shoulder, corresponding to the reversible conversion of Li_2Se to polyselenides and elemental selenium. The broader cathodic peak at 1.9 V became sharp and slightly shifted to 1.97 V in the subsequent cycles as well as the anodic peak, which has been also observed for TiO_2–Se composite,[23] suggesting the presence of electrochemical

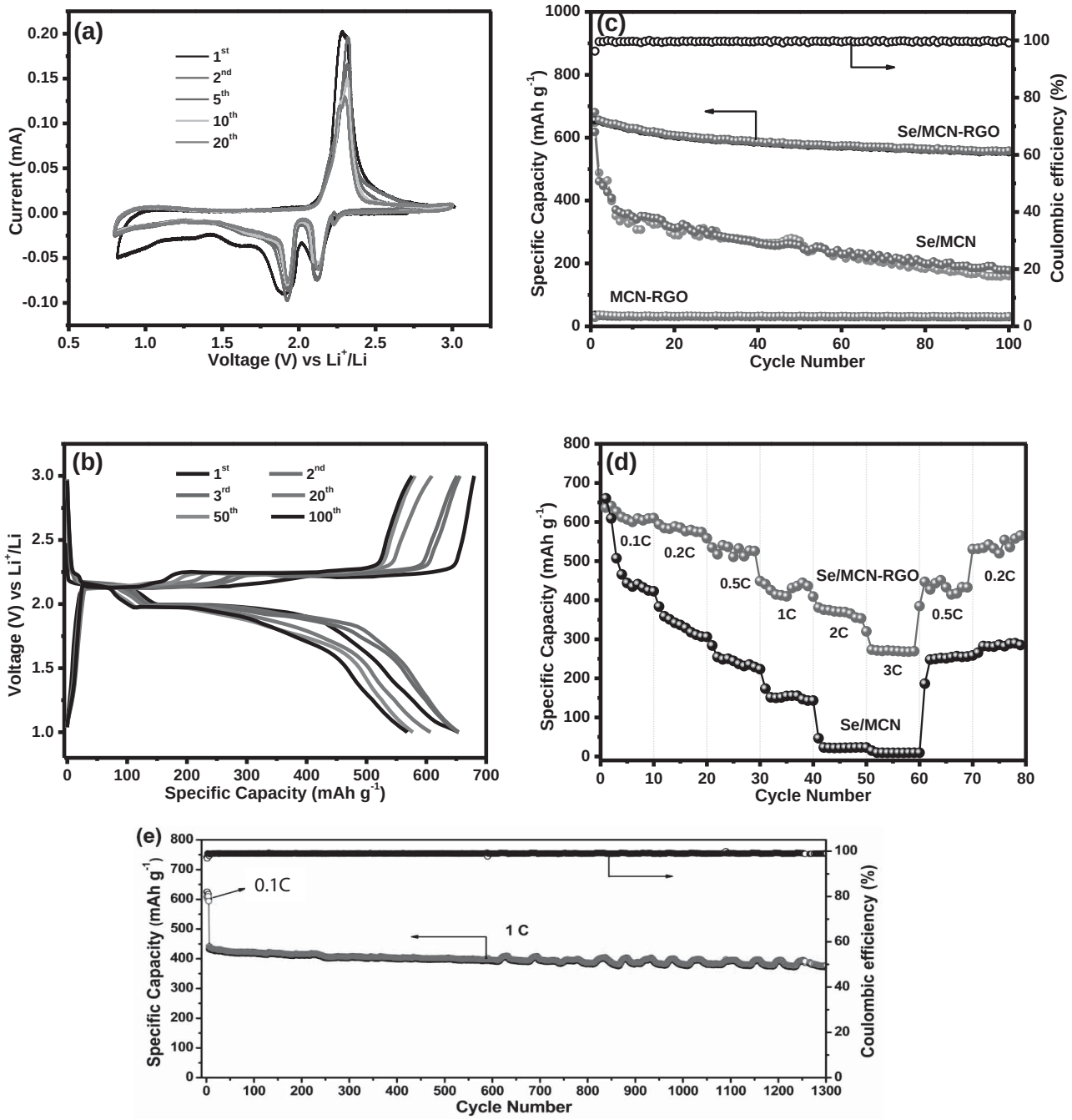

Figure 4. a) CV curves of the 1st, 2nd, 5th, 10th, and 20th cycles for Se/MCN-RGO electrode at a scan rate of 0.1 mV s^{-1}. b) Galvanostatic charge/discharge voltage profiles of the Se/MCN-rGO electrode for the 1st, 2nd, 3rd, 20th, 50th, and 100th cycles. c) Comparison of the cycling performance of Se/MCN-RGO, Se/MCN and MCN-RGO and the Coulombic efficiency of Se/MCN-RGO. For these tests, the cells are cycled between 1.0–3.0 V at a current rate of 0.1 C (1 C = 678 mA g^{-1} Se). d) Rate capability of the Se/MCN-RGO paper electrode and Se/MCN powder electrode at varied current rates of 0.1–3 C. e) Long-term cycling stability of the Se/MCN-RGO electrode (0.1 C for the first five cycles and 1 C for the next 1300 cycles).

activation or stabilization process in the initial cycles, probably due to the redistribution of deposited selenium or Li_2Se in the carbon matrix.[45] The CV curves of 2 to 20 cycles overlap well, indicating the excellent electrochemical stability of the Se/MCN-RGO cathode.

Figure 4b shows the galvanostatic charge/discharge voltage profiles of the Se/MCN-RGO cathode in the different cycles at a current rate of 0.1 C (1 C = 678 mA g^{-1} of Se) between 1.0–3.0 V. There are three voltage plateaus in the discharge process: very short one at 2.25 V, short plateau at 2.15 V, and a long one at about 1.97 V, which could be assigned to the reduction of selenium to different chain length polyselenides and Li_2Se. Two plateaus located at 2.15 V and 2.25 V are observed in the charge process, corresponding to the reverse reactions from

Li_2Se to elemental selenium. Both the charge and discharge voltage plateaus are in good agreement with CV measurements. Moreover, the voltage gap between charge and discharge plateaus for Se/MCN-RGO is much smaller than that for Se/MCN electrode (Figure S6, Supporting Information), and no obvious change of the voltage plateaus is observed even after 100 cycles, corresponding to the low polarization, which further implies the high electrochemical stability and reversibility of the Se/MCN-RGO electrode. The Se/MCN-RGO paper electrode delivered a discharge capacity of 655 mAh g^{-1} with Coulombic efficiency of 96.5% in the first cycle, which corresponds to a 97% capacity utilization of selenium. The comparison of cycling performance for Se/MCN-RGO, Se/MCN and MCN-RGO electrodes at a current rate of 0.1 C between 1.0–3.0 V are shown in Figure 4c. Se/MCN-RGO electrode exhibits better cycling stability with a capacity of 568 mAh g^{-1} after 100 cycles. In contrast, although Se/MCN electrode showed similar initial capacity with Se/MCN-RGO, as high as 620 mAh g^{-1}, the capacity dramatically degraded to ≈300 mAh g^{-1} after 20 cycles and only ≈170 mAh g^{-1} retained after 100 cycles. This capacity fading in Se/MCN is probably induced by dissolution and diffusion of long-chain polyselenides into the ether-based electrolyte, which results in the loss of active material and consequently poor cycling stability.[19] However, for Se/MCN-RGO electrode, the improvement in the cycling performance is mainly attributed to the 3D hierarchical structure constructed by MCN and graphene sheets. The escaped polyselenides from mesopores of MCN could be further adsorbed by graphene sheets, which thus effectively suppresses the shuttling of polyselenides. This is also confirmed by the high Coulombic efficiency for the entire 100 cycles. The MCN-RGO pure carbon matrix was also cycled under same condition as Se/MCN-RGO electrode. It displays a negligible capacity of ≈20 mAh g^{-1} in the voltage range of 1.0–3.0 V, since the lithium intercalation within carbon material mainly occurs at voltage far below 1.0 V,[46,47] indicating that the high capacity in Se/MCN-RGO composite is essentially contributed by active selenium material.

In addition to the good cycling stability, the Se/MCN-RGO electrode also exhibits excellent high-rate capability, as shown in Figure 4d. As the current rate increases from 0.1 to 0.2, 0.5, 1, 2, and 3 C, the electrode displays good capacity retention, varying from 650 to 593, 525, 462, 377, and 274 mAh g^{-1}, respectively. Importantly, the capacity recovers to 478 and 575 mAh g^{-1} when the current rate returns to 0.5 and 0.2 C, indicating the excellent electrochemical reversibility of Se/MCN-RGO composite. Compared to the Se/MCN-RGO, the Se/MCN electrode exhibits poor rate performance. The capacity drops close to 0 when the current rate increases to 2 and 3 C. It also shows severe polarization under the high current rate (**Figure 5**b). While the polarization is significantly improved in Se/MCN-RGO (Figure 5a), suggesting the better electrical and ionic conductivity as a result of the constructed 3D open channels by hierarchical MCN and graphene sheets. For the evaluation of the long-term cycling stability of the Se/MCN-RGO paper electrode, the electrode was cycled at 0.1 C for the first five cycles and then at 1 C for 1300 cycles (Figure 4e). The first cycle at 1 C delivered a discharge capacity of 432 mAh g^{-1} and it retained 385 mAh g^{-1} even after 1300 cycles, corresponding to capacity retention of 89% and a very low capacity degradation

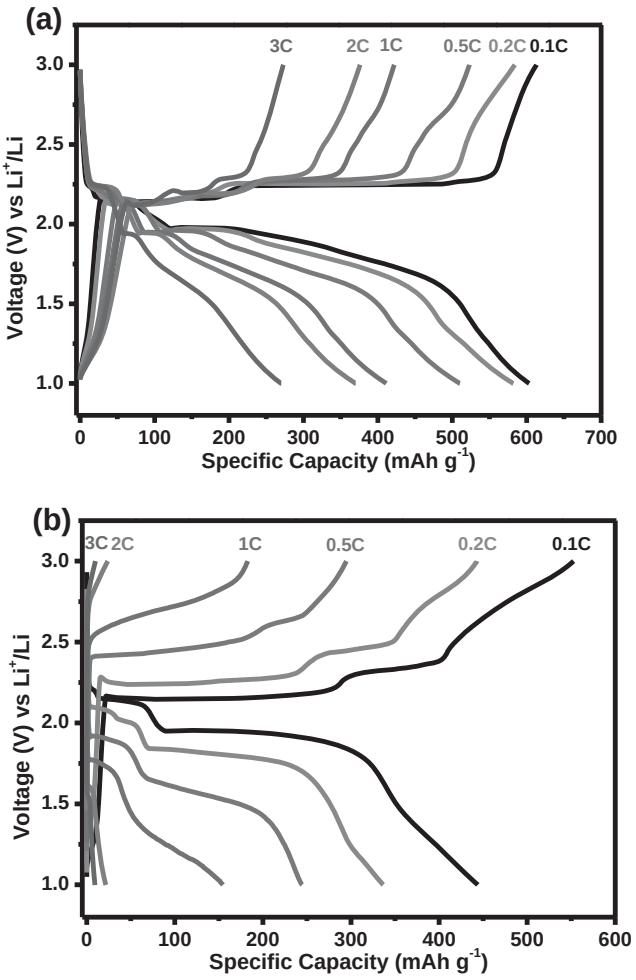

Figure 5. Glavanostatic charge/discharge voltage profiles of a) Se/MCN-RGO and b) Se/MCN electrodes at different current rates from 0.1 to 3 C between 1.0–3.0 V. Higher capacity utilization and reduced polarization with increasing rate are clearly visible in the Se/MCN-RGO paper electrode.

of 0.008% for each cycle. The Coulombic efficiency was close to 100% throughout the cycling. This ultra-long cycling stability demonstrates that the Se/MCN-RGO composite is a promising high capacity and long cycle life cathode material for practical applications.

To better understand the superior electrochemical performance of Se/MCN-RGO, electrochemical impedance spectroscopy (EIS) measurement was performed for the Se/MCN-RGO and Se/MCN electrodes before cycling and after 100 cycles at 0.2 C. As shown in **Figure 6**, the fresh Se/MCN-RGO electrode exhibits lower charge transfer resistance (Rct, determined by the diameter of the semicircle in the high frequency area[48] than Se/MCN electrode, indicating the improved electrical conductivity by incorporation with graphene sheets. After 100 cycles, the Rct for Se/MCN-RGO only shows a slight increase from 452 to 506 Ohm, suggesting the long-cycling stability, whereas the resistance for Se/MCN electrode dramatically increases. The parallel cell EIS test at 20 and 50 cycles further confirm the high electrochemical stability for Se/MCN-RGO (Figure S8,

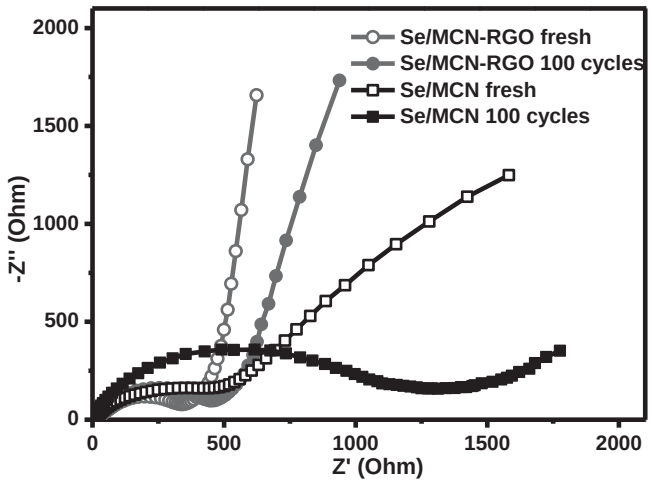

Figure 6. a) Electrochemical impedance spectra of the Se/MCN-RGO and Se/MCN electrodes before and after 100 cycles at current rate of 0.2 C.

Supporting Information). This could be attributed to drastic volume change of the Se/MCN electrode caused by reversible conversion between elemental selenium and Li_2Se during charge/discharge process, which would result in the expansion and shrinkage of electrode and consequently electrical contact lose between active material and conducting carbon matrix.[49] However, in Se/MCN-RGO paper, the flexible graphene sheets could favor the emission of the strain/stress, accommodate volume change and retain the good structural stability during long-cycling, thus giving lower charge transfer resistance.[50] This is further confirmed by the post-cycling FESEM and EDS analysis. **Figure 7** shows that Se/MCN is still well embedded in the graphene sheets and no large agglomerated particles are observed in the Se/MCN-RGO electrode after extended cycling, indicating the high structural stability. The EDS mapping image in Figure 7d shows uniformly distribution of selenium within the carbon matrix in the Se/MCN-RGO paper, with no visible phase segregation even after 1300 charge/discharge cycles (also Figure S9b). Since the cell is finished at the discharge state, small Li_2Se peaks are observed in the XRD patterns from cycled Se/MCN-RGO electrode (**Figure 8**a), which indicates the complete conversion of selenium to Li_2Se during discharge process. However, the intensity of Li_2Se signal is relatively low than (002) carbon peak at ≈26°, which is probably due to the robust confinement of Li_2Se within the carbon matrix.[16] The shift of Se 3p XPS peak to higher binding energy also confirms the presence of Li_2Se in the cycled Se/MCN-RGO paper electrode (Figure 8b).[18]

The high capacity utilization and excellent rate performance as well as the ultra-long cycling stability of the free-standing Se/MCN-RGO paper composite could be primarily attributed to the unique 3D hierarchical architecture. The critical synergic effects of MCN and graphene sheets in improving the electrode performance are threefold. First of all, the hierarchical graphene matrix provides high electronic conductivity and the high chemical diffusivity of Li on graphene plane enhances the transportation of lithium ions for active Se.[51,52] Secondly, the escaped polyselenides from mesopores of MCN could be further adsorbed by graphene sheets, thus suppress the shuttling effect and improve the capacity retention. Finally, with the flexible graphene sheets as a buffer layer, the electrode will not suffer large stress and strain during the de/lithation process and therefore preserves the good electrical contact, contributing to the ultra-long cycle life.

3. Conclusion

In this work, we demonstrate a novel free-standing Se/MCN-RGO paper composite with unique 3D hierarchical architecture as cathode material for high-performance rechargeable Li–Se batteries. The high capacity utilization, excellent rate capability and ultra-long cycling stability have been remarkably achieved. With selenium content of 62% in the electrode, the Se/MCN-RGO delivers initial capacity of 655 mAh g^{-1} (97% of theoretical capacity for Se) and retains 568 mAh g^{-1} after 100 cycles. It also exhibits ultra-long cycle life with a stable capacity of about 400 mAh g^{-1} for 1300 cycles at 1 C rate. These results demonstrate that the Se/MCN-RGO composite is a promising high capacity and long cycle life cathode material for rechargeable lithium batteries in practical application. Furthermore, the concept of such 3D hierarchical architecture and synthesis strategy would be easily expanded to other materials for advanced energy storage systems, such as silicon for Li-ion batteries and metal oxides for supercapacitors.

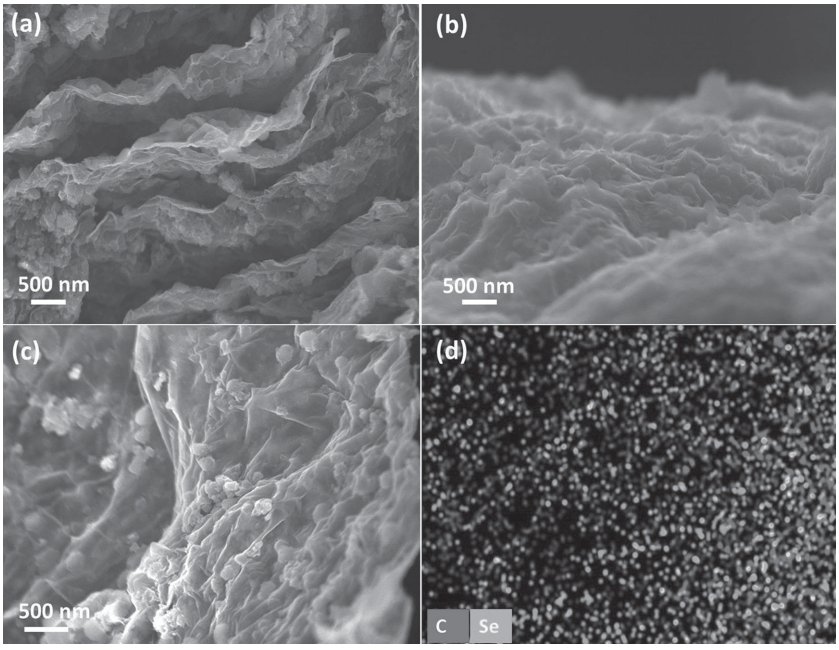

Figure 7. FESEM images of a) cross-section, b,c) surface, and d) EDS carbon (red) and selenium (green) element mapping image of the Se/MCN-RGO electrode after 1300 charge/discharge cycles.

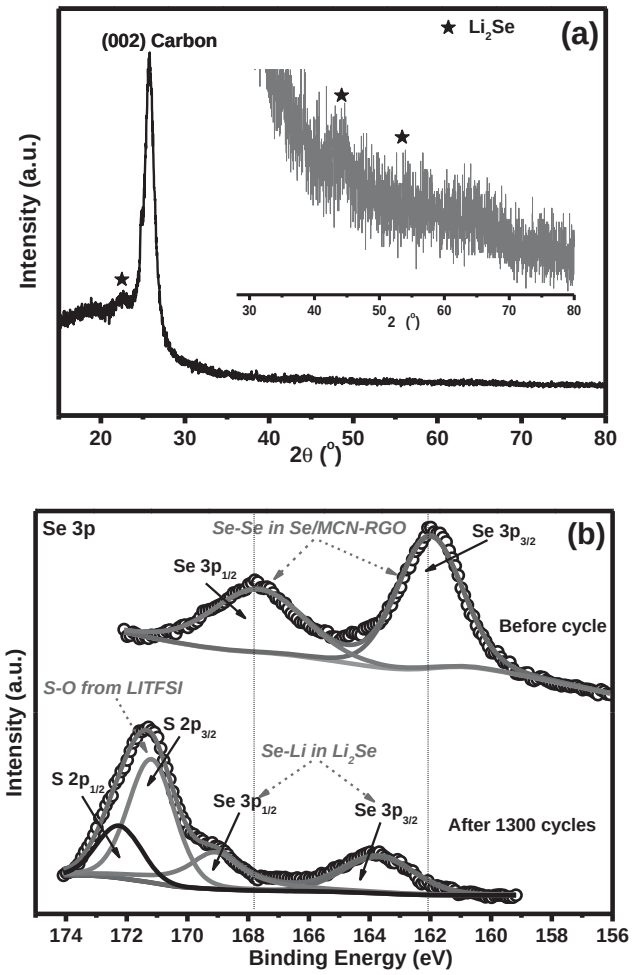

Figure 8. a) XRD pattern of the Se/MCN-RGO paper after 1300 charge/discharge cycles. Inset: zoom-in pattern for 2θ range of 30–80°. b) High-resolution XPS Se 3p spectra of the Se/MCN-RGO paper before and after 1300 charge/discharge cycles.

4. Experimental Section

Material Synthesis: The graphite powder was purchased from Alfa Aesar. Selenium and mesoporous carbon nanoparticles (MCN) were from Sigma-Aldrich. All the chemicals were used as received without further treatment. The water used was deionized water with a resistivity of 18 MΩ cm^{-1} and other solvent are analytical grade. Graphene oxide (GO) was synthesized from flake graphite powder using a modified Hummers method in a two oxidation steps (See details in Supporting Information).[53] The as-prepared GO was stored in an aqueous suspension (5 mg mL^{-1}) and normally exfoliated by 1 h sonication before use. The Se/MCN powder composite was typically synthesized as following: selenium and MCN were wet ball-milling mixed for 72 h at weight ratio of 75:25 in acetone. After drying at 50 °C in an oven for 2h to evaporate residual acetone, the mixed selenium and MCN powders (Se-MCN) were heating at 260 °C for 20 h under argon atmosphere to obtain Se/MCN composite. Next, 35 mg Se/MCN powders were dispersed in 6 mL DI water/ethanol (1:1 v) mixed solvent by sonicating for 1 h. 3 mL GO aqueous suspension (15 mg GO) was drop-wise added into the Se/MCN suspension and following sonicated for 1 h. The Se/MCN-GO mixed suspension was in black color and could be stored for 1 month without precipitation. The total solid concentration in Se/MCN-GO suspension was ≈5.5 mg mL^{-1}. To get the free-standing Se/MCN-GO paper, 4 mL Se/MCN-GO suspension was vacuum filtrated with anodic aluminum oxide (AAO) membrane (Whatman, 0.2 μm pore size, 47 mm diameter). The obtained paper was then punched out into several circular disks with diameter of 1 cm. Subsequently, the circular disks were put into a small glass vial, which was further placed in a big glass bottle containing 2 mL of hydrazine monohydrate, without direct contact between the samples and hydrazine monohydrate. After sealing, the glass bottle was kept at 130 °C for 3 h to reduce GO by hydrazine vapor. Following cool down, the paper disks were gently washed with DI water twice to remove the adsorbed hydrazine and dried in air at room temperature overnight. Finally, the paper disks were heating at 200 °C for 10 h in a flow of argon to obtain Se/MCN-RGO paper. For comparison, MCN-RGO paper was also prepared at a weight ratio of 1:1 (MCN to GO) under the same condition without selenium.

Materials Characterization: The microstructures and morphologies of the obtained samples were characterized by Hitachi SU-8030 field emission scanning electron microscopy (FESEM) and JEOL 2100 transmission electron microscope (TEM) with an energy dispersive spectroscopy (EDS) detector. X-ray diffraction (XRD) were examined using the Scintag XDS 2000 diffractometer (Cu Kα, λ = 1.5418 Å). Raman spectra were measured on an Acton TriVista CRS Confocal Raman System (514.5 nm) with Ar-ion laser as an excitation source. Nitrogen sorption isotherms were performed on ASAP 2010 system (Micrometitics Inc.) X-ray photoelectron spectroscopy (XPS) was conducted by Thermo Scientific ESCALAB 250Xi equipped with an electron flood gun and a scanning ion gun, using the Al Kα radiation (1486.6 eV) as the excitation source. The binding energy scale was calibrated with respect to adventitious carbon (C1s). Thermogravimetric analyses (TGA) were measured on TGA/SDTA851e analyzer (Mettler Toledo) at a heating rate of 10 °C min^{-1} in argon from 30 to 600 °C.

Electrochemical Measurements: Electrochemical performance was evaluated using two-electrode 2032-type coin cell paired with lithium metal as counter electrode at room temperature. The free-standing Se/MCN-RGO paper and controlled sample MCN-RGO were directly used as working electrode without any further treatment. For Se/MCN electrode, the Se/MCN powders, super P carbon black, and poly (vinylidene fluoride) (PVDF) binder at weight ratio 80:10:10 were mixed into a slurry in N-methyl pyrrolidone (NMP) using mortar and the slurry was casting on Al foil for test. The typical mass loading of selenium active material in the paper and the casting electrode is ≈1.2 mg cm^{-2}. The electrolyte was a solution of 1 M lithium bis(trifluoromethanesulfonyl) imide (LITFSI) dissolved in dimethoxyethane: 1,3 dioxolane (DME:DOL, 1:1 by volume) and the separator was glass fiber (GF/F, Whatman). The coin-cells were assembled in an argon-filled glove box (H_2O, O_2 < 0.5 ppm). The galvanostatic charge and discharge were tested on an Arbin BT2000 system in the voltage range of 1.0–3.0 V versus Li^+/Li. Cyclic voltammogram (CV) was performed using the Solartron 1260/1287 electrochemical interface at a scan rate of 0.1 mV s^{-1} between 0.8–3.0 V. Electrochemical impedance data (EIS) were collected on a Solartron 1260 impedance analyzer coupled with a Solartron 1286 electrochemical interface by applying an AC voltage of 10 mV amplitude and DC open circuit voltage in the frequency range of 100 kHz to 0.1 Hz at room temperature. The current rate and specific capacity were calculated based on the weight of selenium.

Supporting Information

Supporting Information is available from the Wiley Online Library or from the author.

Acknowledgements

This work was partially supported by National Natural Science Foundation of China (21276284). K.H. acknowledges funding support

from China Scholarship Council and Hunan Provincial Innovation Foundation for Postgraduate.

Received: August 17, 2014
Revised: September 21, 2014
Published online: November 20, 2014

[1] J. M. Tarascon, M. Armand, *Nature* **2001**, *414*, 359.
[2] N. S. Choi, Z. Chen, S. A. Freunberger, X. Ji, Y. K. Sun, K. Amine, G. Yushin, L. F. Nazar, J. Cho, P. G. Bruce, *Angew. Chem. Int. Ed.* **2012**, *51*, 9994.
[3] M. M. Thackeray, C. Wolverton, E. D. Isaacs, *Energy Environ. Sci.* **2012**, *5*, 7854.
[4] M. S. Whittingham, *Chem. Rev.* **2004**, *104*, 4271.
[5] V. Etacheri, R. Marom, R. Elazari, G. Salitra, D. Aurbach, *Energy Environ. Sci.* **2011**, *4*, 3243.
[6] A. Manthiram, *J. Phys. Chem. Lett.* **2011**, *10*, 176.
[7] P. G. Bruce, S. A. Freunberger, L. J. Hardwick, J. M. Tarascon, *Nat. Mater.* **2011**, *11*, 19.
[8] X. Ji, L. F. Nazar, *J Mater. Chem.* **2010**, *20*, 9821.
[9] A. Manthiram, Y. Fu, Y.-S. Su, *Acc. Chem. Res.* **2013**, *46*, 1125.
[10] J. B. Goodenough, Y. Kim, *Chem. Mater.* **2009**, *22*, 587.
[11] F. Li, T. Zhang, H. Zhou, *Energy Environ. Sci.* **2013**, *6*, 1125.
[12] Y. Yang, G. Zheng, Y. Cui, *Chem. Soc. Rev.* **2013**, *42*, 3018.
[13] Y. X. Yin, S. Xin, Y. G. Guo, L. J. Wan, *Angew. Chem. Int. Ed.* **2013**, *52*, 13186.
[14] T. K. Todorov, K. B. Reuter, D. B. Mitzi, *Adv. Mater.* **2010**, *22*, E156.
[15] J. Qian, K. J. Jiang, J. H. Huang, Q. S. Liu, L. M. Yang, Y. Song, *Angew. Chem. Int. Ed.* **2012**, *51*, 10351.
[16] C.-P. Yang, S. Xin, Y.-X. Yin, H. Ye, J. Zhang, Y.-G. Guo, *Angew. Chem. Int. Ed.* **2013**, *52*, 1.
[17] C. Luo, Y. Zhu, Y. Wen, J. Wang, C. Wang, *Adv. Funct. Mater.* **2014**, *24*, 4082.
[18] Y. Cui, A. Abouimrane, J. Lu, T. Bolin, Y. Ren, W. Weng, C. Sun, V. A. Maroni, S. M. Heald, K. Amine, *J. Am. Chem. Soc.* **2013**, *135*, 8047.
[19] A. Abouimrane, D. Dambournet, K. W. Chapman, P. J. Chupas, W. Weng, K. Amine, *J. Am. Chem. Soc.* **2012**, *134*, 4505.
[20] Y. Cui, A. Abouimrane, C. J. Sun, Y. Ren, K. Amine, *Chem. Commun.* **2014**, *50*, 5576.
[21] C. Luo, Y. Xu, Y. Zhu, Y. Liu, S. Zheng, Y. Liu, A. Langrock, C. Wang, *ACS Nano* **2013**, *7*, 8003.
[22] L. Liu, Y. Hou, Y. Yang, M. Li, X. Wang, Y. Wu, *RSC Adv.* **2014**, *4*, 9086.
[23] Z. Zhang, X. Yang, X. Wang, Q. Li, Z. Zhang, *Solid State Ionics* **2014**, *260*, 101.
[24] Z. Zhang, Z. Zhang, K. Zhang, X. Yang, Q. Li, *RSC Adv.* **2014**, *4*, 15489.
[25] L. Liu, Y. Hou, X. Wu, S. Xiao, Z. Chang, Y. Yang, Y. Wu, *Chem. Commun.* **2013**, *49*, 11515.
[26] D. Kundu, F. Krumeich, R. Nesper, *J. Power Sources* **2013**, *236*, 112.
[27] X. Wang, Q. Qu, Y. Hou, F. Wang, Y. Wu, *Chem. Commun.* **2013**, *49*, 6179.
[28] X. Wang, Y. Hou, Y. Zhu, Y. Wu, R. Holze, *Sci. Rep.* **2013**, *3*, 1401.
[29] R. Chen, T. Zhao, J. Lu, F. Wu, L. Li, J. Chen, G. Tan, Y. Ye, K. Amine, *Nano Lett.* **2013**, *13*, 4642.
[30] S. Chen, X. Huang, H. Liu, B. Sun, W. Yeoh, K. Li, J. Zhang, G. Wang, *Adv. Energy Mater.* **2014**, *4*, 1301761.
[31] J. Schuster, G. He, B. Mandlmeier, T. Yim, K. T. Lee, T. Bein, L. F. Nazar, *Angew. Chem. Int. Ed.* **2012**, *51*, 3591.
[32] C. K. Chan, H. Peng, G. Liu, K. McIlwrath, X. F. Zhang, R. A. Huggins, Y. Cui, *Nat. Nanotechnol.* **2007**, *3*, 31.
[33] X. Zhou, Y.-X. Yin, L.-J. Wan, Y.-G. Guo, *Adv. Energy Mater.* **2012**, *2*, 1086.
[34] Z. Wei Seh, W. Li, J. J. Cha, G. Zheng, Y. Yang, M. T. McDowell, P. C. Hsu, Y. Cui, *Nat. Commun.* **2013**, *4*, 1331.
[35] X. Ji, K. T. Lee, L. F. Nazar, *Nat. Mater.* **2009**, *8*, 500.
[36] W. Weng, V. G. Pol, K. Amine, *Adv. Mater.* **2013**, *25*, 1608.
[37] S. Pei, J. Zhao, J. Du, W. Ren, H.-M. Cheng, *Carbon* **2010**, *48*, 4466.
[38] X. Zhou, L. J. Wan, Y. G. Guo, *Adv. Mater* **2013**, *25*, 2152.
[39] X. Wang, Z. Zhang, Y. Qu, Y. Lai, J. Li, *J. Power Sources* **2014**, *256*, 361.
[40] F. Sun, J. Wang, H. Chen, W. Li, W. Qiao, D. Long, L. Ling, *ACS Appl. Mater. Interfaces* **2013**, *5*, 5630.
[41] J. Song, T. Xu, M. L. Gordin, P. Zhu, D. Lv, Y.-B. Jiang, Y. Chen, Y. Duan, D. Wang, *Adv. Funct. Mater.* **2014**, *24*, 1243.
[42] X. G. Sun, X. Wang, R. T. Mayes, S. Dai, *ChemSusChem* **2012**, *5*, 2079.
[43] G. He, X. Ji, L. Nazar, *Energy Environ. Sci.* **2011**, *4*, 2878.
[44] X. Zhou, J. Xie, J. Yang, Y. Zou, J. Tang, S. Wang, L. Ma, Q. Liao, *J. Power Sources* **2013**, *243*, 993.
[45] C. Zu, Y. Fu, A. Manthiram, *J. Mater. Chem. A* **2013**, *1*, 10362.
[46] N. A. Kaskhedikar, J. Maier, *Adv. Mater.* **2009**, *21*, 2664.
[47] S. Liu, Z. Wang, C. Yu, H. B. Wu, G. Wang, Q. Dong, J. Qiu, A. Eychmuller, X. W. David Lou, *Adv. Mater.* **2013**, *25*, 3462.
[48] A. Konarov, D. Gosselink, T. N. L. Doan, Y. Zhang, Y. Zhao, P. Chen, *J. Power Sources* **2014**, *259*, 183.
[49] X. He, J. Ren, L. Wang, W. Pu, C. Jiang, C. Wan, *J. Power Sources* **2009**, *190*, 154.
[50] Y. Shi, J. Z. Wang, S. L. Chou, D. Wexler, H. J. Li, K. Ozawa, H. K. Liu, Y. P. Wu, *Nano Lett.* **2013**, *13*, 4715.
[51] Y. Shi, S.-L. Chou, J.-Z. Wang, D. Wexler, H.-J. Li, H.-K. Liu, Y. Wu, *J. Mater. Chem.* **2012**, *22*, 16465.
[52] V. A. S. K. Persson, L. J. Hardwick, Y. Hinuma, A. v. d. V. Ying Shirley Meng, G. Ceder, *J. Phys. Chem. Lett* **2010**, *1*, 1176.
[53] K. Han, J. Shen, C. M. Hayner, H. Ye, M. C. Kung, H. H. Kung, *J. Power Sources* **2014**, *251*, 331.